Multidimensional material response simulations of a full-scale tiled ablative heatshield

Jeremie B. E. Meurisse[a,*], Jean Lachaud[b], Francesco Panerai[c], Chun Tang[d], Nagi N. Mansour[d]

[a]*STC at NASA Ames Research Center, Moffett Field, CA 94035, USA*
[b]*C la Vie, Noumea, 98800, New Caledonia*
[c]*AMA Inc. at NASA Ames Research Center, Moffett Field, CA 94035, USA*
[d]*NASA Ames Research Center, Moffett Field, CA 94035, USA*

Abstract

The Mars Science Laboratory (MSL) was protected during Mars atmospheric entry by a 4.5 meter diameter heatshield, which was constructed by assembling 113 thermal tiles made of NASA's flagship porous ablative material, Phenolic Impregnated Carbon Ablator (PICA). Analysis and certification of the tiles thickness were based on a one-dimensional model of the PICA response to the entry aerothermal environment. This work provides a detailed three-dimensional heat and mass transfer analysis of the full-scale MSL tiled heatshield. One-dimensional and three-dimensional material response models are compared at different locations of the heatshield. The three-dimensional analysis is made possible by the use of the Porous material Analysis Toolbox based on OpenFOAM (PATO) to simulate the material response. PATO solves the conservation equations of solid mass, gas mass, gas momentum and total energy, using a volume-averaged formulation that includes production of gases from the decomposition of polymeric matrix. Boundary conditions at the heatshield forebody surface were interpolated in time and space from the aerothermal environment computed with the Data Parallel Line Relaxation (DPLR) code at discrete points of the MSL trajectory. A mesh consisting of two million cells was

created in Pointwise, and the material response was performed using 840 processors on NASA's Pleiades supercomputer. The present work constitutes the first demonstration of a three-dimensional material response simulation of a full-scale ablative heatshield with tiled interfaces. It is found that three-dimensional effects are pronounced at the heatshield outer flank, where maximum heating and heat loads occur for laminar flows.

Nomenclature

$\mathcal{A}_{i,j}$ Arrhenius law pre-exponential factor, $\mathrm{K}^{-n_{i,j}} \cdot \mathrm{s}^{-1}$

$\mathcal{E}_{i,j}$ Arrhenius law activation energy, $\mathrm{J} \cdot \mathrm{mol}^{-1}$

$\mathcal{R}$ Perfect gas constant, $\mathrm{J} \cdot \mathrm{mol}^{-1} \cdot \mathrm{K}^{-1}$

$\dot{m}_{ca}$ Char ablation rate, $\mathrm{kg} \cdot \mathrm{m}^{-2} \cdot \mathrm{s}^{-1}$

$\dot{m}_{pg}$ Pyrolysis gas production rate, $\mathrm{kg} \cdot \mathrm{m}^{-2} \cdot \mathrm{s}^{-1}$

St_H Stanton number for heat transfer

St_M Stanton number for mass transfer

$\underline{\underline{\mathbf{K}}}$ Permeability tensor, m^2

$\underline{\underline{\mathbf{k}}}$ Effective thermal conductivity tensor, $\mathrm{W} \cdot \mathrm{m}^{-1} \cdot \mathrm{K}^{-1}$

$\mathbf{n}$ Front surface normal

$\mathbf{v}_g$ Gas velocity, $\mathrm{m} \cdot \mathrm{s}^{-1}$

$\mathbf{v}_{ca}$ Char ablation velocity, $\mathrm{m} \cdot \mathrm{s}^{-1}$

A_k Element k

B' Dimensionless mass blowing rate

C'_H Corrected heat transfer coefficient, $\mathrm{kg} \cdot \mathrm{m}^{-2} \cdot \mathrm{s}^{-1}$

C_H Heat transfer coefficient $= \rho_e u_e St_H$, $\mathrm{kg} \cdot \mathrm{m}^{-2} \cdot \mathrm{s}^{-1}$

C_M Mass transfer coefficient $= \rho_e u_e St_M$, $\mathrm{kg} \cdot \mathrm{m}^{-2} \cdot \mathrm{s}^{-1}$

c_p Specific heat capacity, $\mathrm{J} \cdot \mathrm{kg}^{-1} \cdot \mathrm{K}^{-1}$

e Specific energy, $\mathrm{J} \cdot \mathrm{kg}^{-1}$

$F_{i,j}$ Fraction of subphase j in phase i

h Specific absolute enthalpy, $\mathrm{J} \cdot \mathrm{kg}^{-1}$

K_i Equilibrium constant

$m_{i,j}$ Arrhenius law advancement pyrolysis reaction factor

N_e Number of gaseous elements

N_p Number of solid phases

N_s Number of gaseous species

$n_{i,j}$ Arrhenius law temperature factor

p Pressure, Pa

P_i Number of subphases in solid phase i

q	Heat flux, $\text{W} \cdot \text{m}^{-2}$
S_i	Specie i
T	Temperature, K
x_i	Mole fraction of specie i
x_k	Mole fraction of element k
y_i	Mass fraction of specie i
z_k	Mass fraction of element k

Greek

α	Absorptivity
$\chi_{i,j}$	Advancement of pyrolysis reaction j within phase i
ϵ	Porosity
$\epsilon_{i,0}$	Initial porosity of phase i
λ	Scaling factor for C'_H
μ	Viscosity, $\text{kg} \cdot \text{m}^{-1} \cdot \text{s}^{-1}$
$\nu_{i,k}$	Number of atoms of element k in molecule of specie i
Π	Total pyrolysis gas production rate, $\text{kg} \cdot \text{m}^{-3} \cdot \text{s}^{-1}$
π_k	Pyrolysis gas production rate of specie k, $\text{kg} \cdot \text{m}^{-3} \cdot \text{s}^{-1}$
ρ	Mass density, $\text{kg} \cdot \text{m}^{-3}$
$\rho_{i,0}$	Initial mass density of phase i, $\text{kg} \cdot \text{m}^{-3}$
σ	Stefan-Boltzmann constant, 5.670367×10^{-8} $\text{W} \cdot \text{m}^{-2} \cdot \text{K}^{-4}$
$\underline{\underline{\beta}}$	Klinkenberg correction tensor, $\text{m}^2 \cdot \text{s}^{-1}$
ε	Emissivity
ζ	Mass stoichiometric coefficient

Subscripts

0	Initial
∞	Infinity
a	Ablation
adv	Advection
c	Char
$cond$	Conduction

4

$conv$	Convection
$diff$	Diffusion
e	Boundary layer edge
$flux$	Corrected convection
g	Gas phase
p	Pyrolysis reaction
pla	Plasma
rad	Radiation
s	Solid phase
t	Total (solid and gas phases)
v	Virgin
w	Wall

Superscripts

in	Inside the material
out	Outside the material

1. Introduction

The Mars Science Laboratory (MSL) spacecraft, launched on November 2011, successfully landed the Mars Curiosity rover in the Aeolis Palus region of the Gale Crater on August 2012. The MSL entry vehicle was equipped with a 4.5 m diameter Thermal Protection System (TPS) that effectively protected the spacecraft and its payload during entry into Mars' atmosphere. The MSL TPS used the Phenolic Impregnated Carbon Ablator, or PICA, as heatshield material.[1] PICA is a low density ($\approx$274 kg/m^3) carbon/resin composite, manufactured via impregnation of a rigid carbon fiber preform (FiberForm) with a phenolic resin (Durite$^®$ SC-1008), followed by a proprietary high temperature curing and vacuum drying process.[2] The material was successfully used on the Stardust Sample Return Capsule (SRC), assembled in a 0.8 m diameter monolithic aeroshell.[3] Due to manufacturing constraints, it was unfeasible to construct a 4.5 m diameter heatshield out of a single piece of PICA. Instead, the MSL heatshield was developed as an assembly of 113 PICA tiles containing 23 unique shapes. There were also gaps between the TPS tiles to allow for thermal expansion and contraction. These gaps were filled using a silicone elastomer bonding agent. The MSL heatshield was instrumented with temperature and pressure sensors; therefore, the MSL is an established validation case for ablator response models. The MEDLI (MSL Entry, Descent, and Landing Instrument) suite recorded, among others, time-resolved in-depth temperature data using thermocouple sensors assembled in the MEDLI Integrated Sensor Plugs (MISP). Several studies in the literature have used MISP data as a benchmark for state-of-the-art ablation codes.[4, 5, 6] Modeling of heat and mass transfer in porous materials during atmospheric entry of spacecrafts is a complex and computationally expensive problem. Traditionally, NASA TPS design has been done using one-dimensional ablation and thermal response solvers.[7, 8] Research by Chen and Milos [9, 10] investigated multi-dimensional effects on the thermal response of a monolithic Apollo-shaped heatshield, using the 3dFIAT code developed at the NASA Ames Research Center. The convective aerothermal environment

6

over the exterior TPS surface were derived from the Configuration Based Aerodynamics (CBAERO) analysis of Lunar return trajectories.[11] The analysis indicated that, for a high angle of attack entry, the peak heat flux and heat load are located at the windside heatshield outer flank. At this location, the planar approximation was shown to underpredict the peak bondline temperature. In this study, detailed three-dimensional heat and mass transfer analyses are undertaken on the tiled MSL heatshield to assess the validity and limitations of the traditional one-dimensional design assumption. The Porous material Analysis Toolbox based on OpenFOAM (PATO) software program is used to simulate the TPS response.[12] PATO is released as open source software by NASA.[1] The aerothermal environment at the heatshield surface, at discrete points along the MSL entry trajectory, is obtained from hypersonic Computational Fluid Dynamics (CFD) simulations performed using the Data Parallel Line Relaxation (DPLR)[2] Navier-Stokes software program.[13] A procedure for temporal and spatial interpolation was used to loosely couple the aerothermal environment to the material response. Simulations were performed for both monolithic and tiled heatshield configurations. Tiles are normally not included in 3D material response analysis because of the high computational costs associated with such simulations. The massively parallel simulation support inherited in PATO from its OpenFOAM architecture now makes such studies possible.

The paper is organized as follows. In section 2, we describe the MSL monolithic and tiled heatshield grid used for the simulations. Section 3 presents the governing equations used in the material response model. Section 4 details the spatial and temporal interpolation from DPLR to PATO. In section 5, the overall material response is presented where monolithic and tiles configurations are compared. Detailed heat and mass transfer analyses are undertaken at key locations and compared to one-dimensional simulations to assess multi-dimensional effects. Finally, section 6 presents the conclusion.

---

[1]https://software.nasa.gov/software/ARC-16680-1A
[2]https://software.nasa.gov/software/ARC-16021-1A

2. Computational domain

The MSL aeroshell is a 4.5 m diameter spherically-blunted 70 degree half-angle cone forebody, with triconic afterbody (Fig. 1a). The distribution of the 113 tiles composing the forebody heatshield is presented in Fig. 1b and 1c.

(a) MSL aeroshell.[14]

(b) 113 PICA heatshield tiles.

(c) PICA heatshield side view.
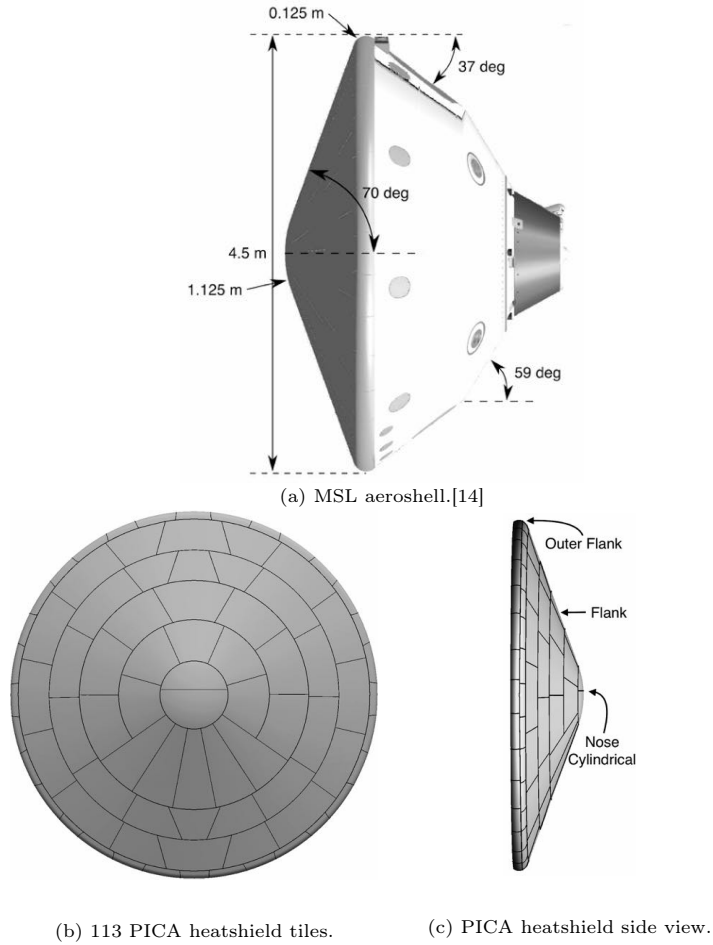
Figure 1: MSL geometry.

The TPS was assembled using a stacking of materials as detailed in [5]. A uniform PICA layer of 31.75 mm thickness was used along the entire heatshield.

8
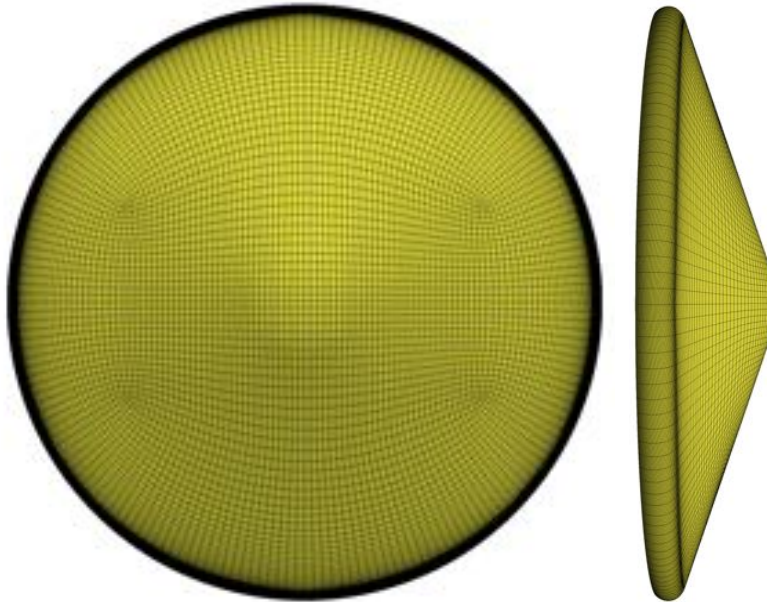
Figure 2: MSL monolithic heatshield mesh.

The heatshield surface geometry used in PATO was extracted from the computational domain used in DPLR. Two PATO computational meshes were generated: a ≈600k cells grid for the monolithic shield configuration (Fig. 2) and a ≈2M cells grid for the tiled configuration (Fig. 3). The minimum cell size is 1 mm for both grids. For the tiled configuration (Fig. 3), the mesh is separated in 2 material regions: porous tiles (yellow) and gap filler between the tiles (orange). In building the computational model for this study, we made the following simplifying assumptions, which will be addressed in follow-up studies. The surface coating applied onto the PICA heatshield and its effects on the material response are neglected. The gap filler, here meshed with two cells of 1 mm each, is assumed to be a non-charring and non-receding phase. Therefore, as opposed to the real case, where the charring process of the gap filler would yield a porous carbonaceous structure, here the interface is impermeable to gases and only conductive heat transfer is allowed through it. The non-receding simplification, also to be refined in future investigations, was inspired by the minimal observed recession during arc-jet testing of the gap filler.[5]
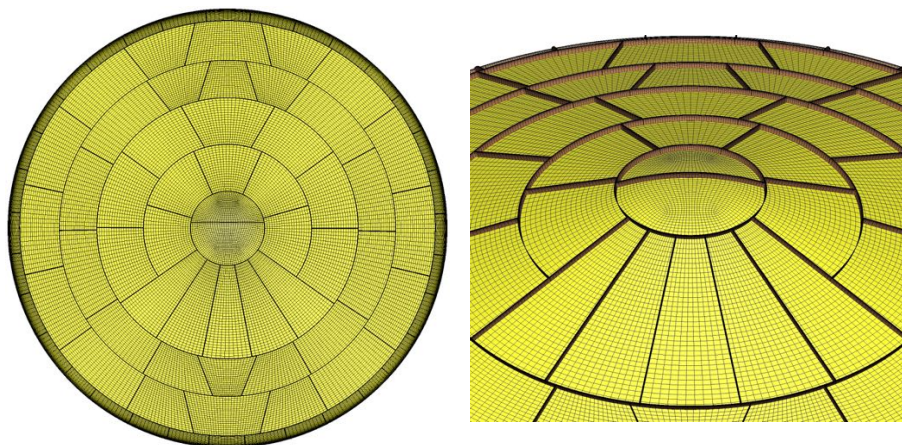
9

Figure 3: MSL tiled heatshield mesh.

3. Computational model

The computational model is a generic heat and mass transfer model for porous reactive materials containing several solid phases and a single gas phase.[15] The detailed chemical interactions occurring between the solid phases and the gas phase are modeled at the pore scale assuming local thermal equilibrium: solid pyrolysis, pyrolysis species injection in the gas phase, heterogeneous reactions between the solid phases and the gas phase, and homogeneous reactions in the gas phase. The chemistry models are integrated in a macroscopic model derived by volume-averaging the governing equations for the conservation of solid mass, gas mass, species (finite-rate chemistry) or elements (equilibrium chemistry), momentum, and energy. This generic model is implemented in the Porous material Analysis Toolbox based on OpenFOAM (PATO) [12], a C++ top level module of the open source (GNU GPL) computational fluid dynamics software program OpenFOAM. The open source (GNU LGPL) third party library Mutation++, produced by the von Karman Institute for Fluid Dynamics, is dynamically linked to compute equilibrium chemistry compositions and thermodynamic and transport properties.[16] Gas surface interactions are modeled using equilibrium chemistry models that are preferred for design due to the lack of reliability of available finite-rate chemistry models and data. The

10

equilibrium chemistry model of PATO has been shown to perfectly reproduce one-dimensional design tool results.[17] PATO has been carefully verified against the Fully Implicit Ablation and Thermal Analysis (FIAT) software, NASA's state-of-the-art-code for TPS response modeling, extensively validated through arcjet tests and flight data.[6] For convenience, the governing equations of the equilibrium model are stated in sections 3.1, 3.2 and 3.3. In particular, the material response model and input data are presented together for clarity. In addition to this section, Appendix A details the associated surface boundary conditions.

For this study, the Theoretical Ablative Composite for Open Testing (TACOT) database developed by the TPS community was used to define the porous material properties.[3] TACOT is a fictitious material that was inspired from PICA-class, low density carbon/phenolic ablators using realistic material properties found in the literature. Subtle differences were observed when running the same analyses using proprietary PICA data, but the overall trends were consistent.

3.1. Mass conservation

The gaseous mass conservation equation includes a production term on the right hand side to account for pyrolysis gas production. This is formulated in section 3.4. Mass conservation reads

$$\partial_t \left(\epsilon_g \rho_g \right) + \partial_{\mathbf{x}} \cdot \left(\epsilon_g \rho_g \mathbf{v}_g \right) = \Pi \tag{1}$$

The pyrolysis gas flow rate at the heatshield front surface $\dot{m}_{pg}$ is given by

$$\dot{m}_{pg} = \epsilon_g \rho_g \mathbf{v}_g \cdot \mathbf{n} \tag{2}$$

where $\mathbf{n}$ is the heatshield front surface normal.

---

[3] http://ablation2015.engineering.uky.edu/files/2014/02/TACOT_3.0.xls

3.2. Momentum conservation

The volume-averaged momentum conservation for the porous medium is formulated as

$$\mathbf{v}_g = -\frac{1}{\epsilon_g} \left(\frac{1}{\mu} \underline{\underline{\mathbf{K}}} + \frac{1}{p_g} \underline{\underline{\beta}} \right) \cdot \partial_{\mathbf{x}} p_g \tag{3}$$

where $\underline{\underline{\mathbf{K}}}$ is the intrinsic permeability tensor and $\underline{\underline{\beta}}$ is the Klinkenberg correction to the effective permeability tensor that accounts for slip effects at the pore scale when the Knudsen number is large.[18, 19] The virgin and char material permeabilities ($\underline{\underline{\mathbf{K_v}}}$ and $\underline{\underline{\mathbf{K_c}}}$) and $\underline{\underline{\beta}}$ are second order tensors for transverse isotropic materials like PICA and TACOT. In the present work, we neglected the Klinkenberg correction and the material anisotropy (Table 1). Virgin and char material porosities (ϵ_{gv} and ϵ_{gc}) are also included in the table.

Table 1: Material properties for the average momentum conservation equation

$\underline{\underline{\mathbf{K_v}}}$ [m^2]	$\underline{\underline{\mathbf{K_c}}}$ [m^2]	$\epsilon_{gv}[-]$	$\epsilon_{gc}[-]$	$\underline{\underline{\beta}}$ [m^2/s]
1.6e-11 $\underline{\underline{\mathbf{I}}}$	2e-11 $\underline{\underline{\mathbf{I}}}$	0.8	0.85	$\underline{\underline{\mathbf{0}}}$

3.3. Energy conservation

Under the local thermal equilibrium assumption, the energy conservation is written as

$$\partial_t(\rho_t e_t) + \partial_{\mathbf{x}} \cdot (\epsilon_g \rho_g h_g \mathbf{v}_g) = \partial_{\mathbf{x}} \cdot (\underline{\underline{\mathbf{k}}} \cdot \partial_{\mathbf{x}} T) \tag{4}$$

where the total storage energy e_t of the porous medium is the sum of the energy of its phases

$$\rho_t e_t = \epsilon_g \rho_g e_g + \sum_{i \in [1, N_p]} \epsilon_i \rho_i h_i \tag{5}$$

Effective thermal conductivity is generally the main mode of heat transport. To solve Eq. 4, it is more convenient to express it in terms of temperature as follows

12

$$\sum_{i \in [1,N_p]} \left[\left(\epsilon_i \rho_i c_{p,i} \right) \partial_t T \right] - \partial_{\mathbf{x}} \cdot \left(\underline{\underline{\mathbf{k}}} \cdot \partial_{\mathbf{x}} T \right) =$$
$$- \sum_{i \in [1,N_p]} \left[h_i \partial_t (\epsilon_i \rho_i) \right] - \partial_t (\epsilon_g \rho_g h_g - \epsilon_g p_g) + \partial_{\mathbf{x}} \cdot (\epsilon_g \rho_g h_g \mathbf{v}_g) \tag{6}$$

and implicitly solve for temperature.[15]

Figure 4 shows the virgin and char effective thermal conductivities (k_v and k_c) of TACOT used in this study. Virgin and char specific heat capacities ($c_{p,v}$ and $c_{p,c}$) and enthalpies (h_v and h_c) are plotted in Fig. 5.
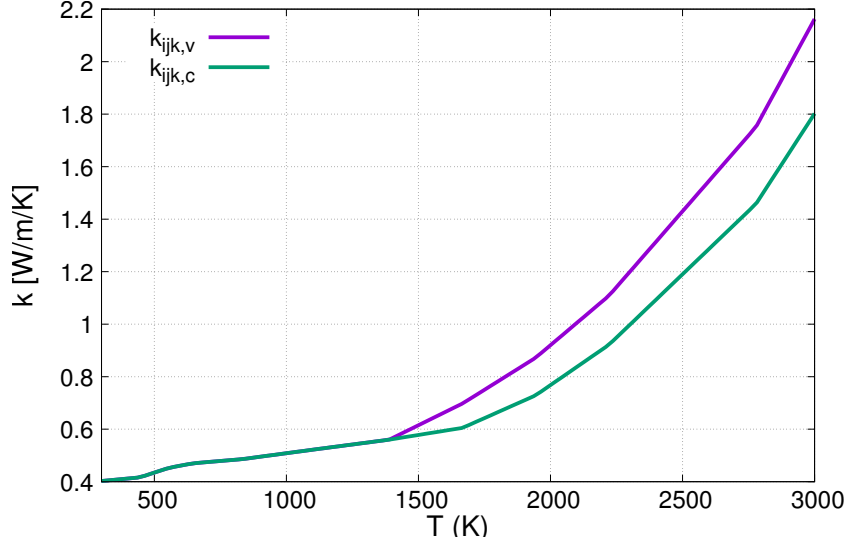
Figure 4: **Virgin and char effective thermal conductivities.**

3.4. Pyrolysis

Each phase i is split into subphases j to model different decomposition mechanisms. The decomposition is written in the following form

$$p_{i,j} \longrightarrow \sum_{k \in [1,N_e]} \zeta_{i,j,k} A_k, \quad \forall\, i \in [1, N_p], \forall\, j \in [1, P_i]. \tag{7}$$
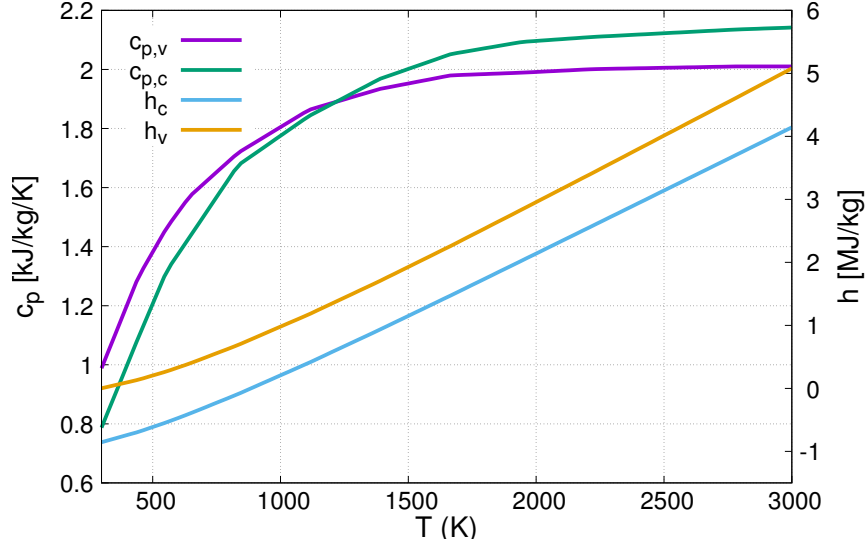
Figure 5: Virgin and char material specific heat capacities and enthalpies.

Here, the subphase j of solid phase i produces element A_k at the stoichiometric proportion given by the coefficients $\zeta_{i,j,k}$.

The TACOT model used in the study has two solid phases: the fibers ($i = 1$) and the matrix ($i = 2$). The fibers of the PICA substrate do not decompose; therefore, only the parameters of the matrix phase are needed. The pyrolysis of the matrix phase is modeled with the coefficients given in Table 2, for three matrix subphases. Constant stoichiometric coefficients are used in the base PICA and TACOT models; therefore, it is not necessary to solve the element conservation equation (Eq. 15 in [15]) in the present study.

Table 2: Pyrolysis reactions for this MSL heatshield simulation

Pyrolysis reaction $p_{i,j}$	Phase i	Element A_k	Stoichiometric coefficient $\zeta_{i,j,k}$
$p_{2,1}$	Matrix	$[C, H, O]$	$[0.495,\ 0.13691,\ 0.36809]$
$p_{2,2}$	Matrix	$[C, H, O]$	$[0.495,\ 0.13691,\ 0.36809]$
$p_{2,3}$	Matrix	$[C, H, O]$	$[0.495,\ 0.13691,\ 0.36809]$

The pyrolysis reaction advancement $\chi_{i,j}$ (with $0 < \chi_{i,j} < 1$) of $p_{i,j}$ is formu-

14

lated using the following Arrhenius form

$$\partial_t \chi_{i,j} = (1 - \chi_{i,j})^{m_{i,j}} \, T^{n_{i,j}} \mathcal{A}_{i,j} \exp\left(-\frac{\mathcal{E}_{i,j}}{\mathcal{R}T}\right), \quad \forall \, i \in [1, N_p], \, \forall \, j \in [1, P_i]. \quad (8)$$

The pyrolysis gas production rate of element k by decomposition of the solid is obtained by summation of the productions of the N_p phases.

$$\pi_k = \sum_{i \in [1, N_p]} \sum_{j \in [1, P_i]} \zeta_{i,j,k} \, \epsilon_{i,0} \, \rho_{i,0} \, F_{i,j} \, \partial_t \, \chi_{i,j} \quad (9)$$

Table 3 and 4 provide the parameters for Eqs. 8 and 9 used in the present work.

Table 3: Initial porosity and density

Phase i	$\epsilon_{i,0}$ $[-]$	$\rho_{i,0}$ $[\text{kg/m}^3]$
Fiber	0.1	1600
Matrix	0.1	1200

Table 4: Pyrolysis reaction factors

Reaction $p_{i,j}$	$F_{i,j}$ $[-]$	$\mathcal{A}_{i,j}$ $[\text{K}^{-n_{i,j}}/\text{s}]$	$\mathcal{E}_{i,j}$ $[\text{J/mol}]$	$m_{i,j}$ $[-]$	$n_{i,j}$ $[-]$
$p_{2,1}$	0.25	12000	71130.89	3	0
$p_{2,2}$	0.19	4.98e8	1.7e5	3	0
$p_{2,3}$	0.06	4.98e8	1.7e5	3	0

The overall pyrolysis gas production rate is obtained by summing over the elements k as

$$\Pi = -\partial_t(\epsilon_m \rho_m) = \sum_{k \in [1, N_e]} \pi_k \quad (10)$$

Figure 6 shows the temperature and the mass loss evolution in time for a constant heating rate. The mass loss is expressed as the solid mass density ρ_s over the virgin solid mass density ρ_{sv}. Figure 7 shows the pyrolysis gas production rates of each element.
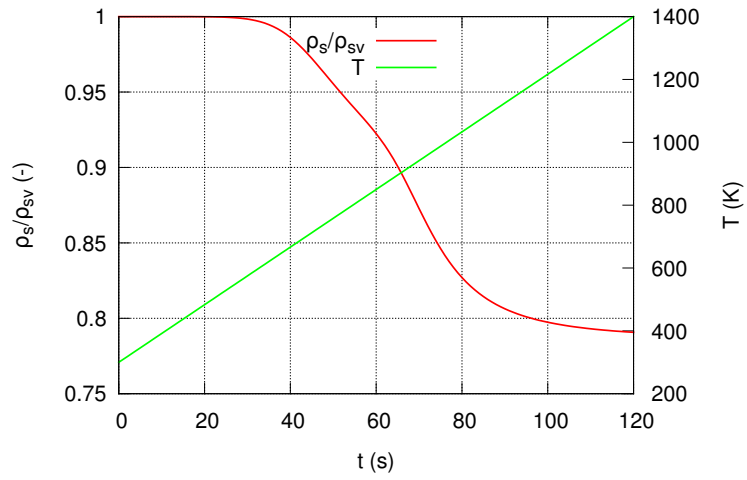
15

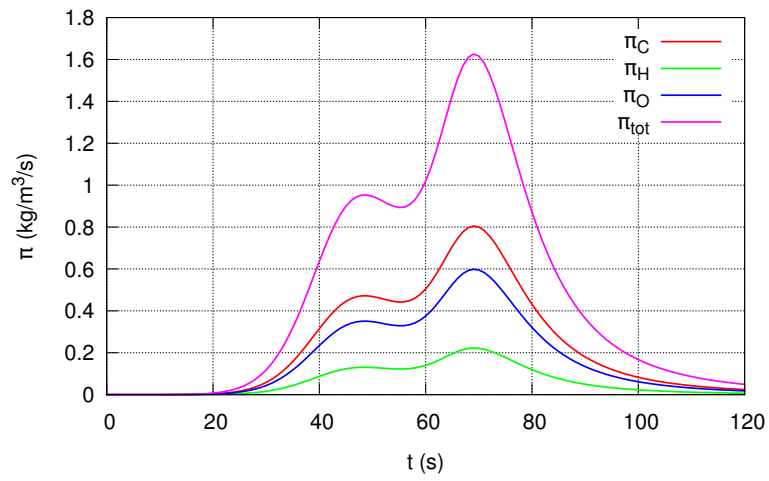**Figure 6: Pyrolysis gas mass loss and temperature.**

Figure 7: Pyrolysis gas production rates.

16

4. Aerothermal environment

DPLR simulations were performed to provide surface boundary conditions for PATO. The capability of DPLR in accurately predicting the flow field around a Mars entry capsule was demonstrated during past investigations.[20] For the present work, the MSL flight environment was simulated under the following assumptions:

- Laminar boundary layer.

- Chemical non-equilibrium.

- Thermal non-equilibrium.

- Radiative equilibrium: $\varepsilon = 0.89$.

- Super-catalytic wall boundary condition: CO_2 and N_2 full recombination.

- Non-blowing and smooth wall.

- Mars atmosphere: $y_{CO_2} \approx 0.97$ & $y_{N_2} \approx 0.03$.

- 8 species and 12 reactions.[21]
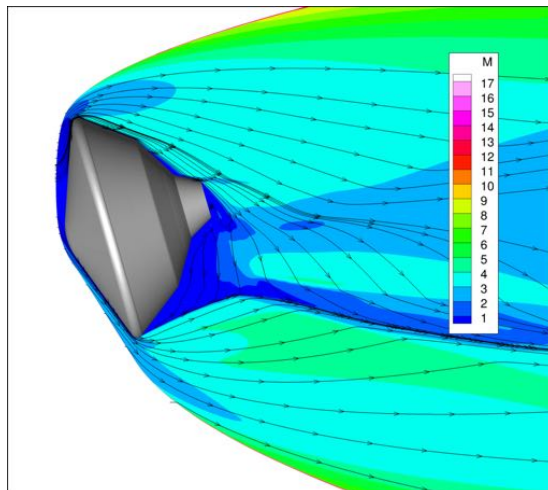
Figure 8: MSL environment from DPLR.

Figure 8 shows the Mach number contour at the pitch plane for the MSL environment computed at 76.2 s after Entry Interface. Simulations were performed at 11 discrete times along the MSL 08-TPS-02/01a trajectory: 48.4, 59.1, 64.4, 69.6, 71.5, 73.9, 76.2, 80.5, 84.4, 87.5 and 100.5 s. The numerical results from DPLR were post-processed using the BLAYER[4] code to determine the Boundary Layer Edge (BLE) properties using a curvature-based method. Figure 9 shows the CFD mesh used in BLAYER. From the BLAYER results, PATO used the following flow quantities to perform the material response: wall pressure, heat transfer coefficient, and BLE enthalpy. The shear stresses at the surface are omitted. Figure 10 shows the location of the MISP sensor plugs on the MSL heatshield. Each MISP carried thermocouple sensors (labelled as TC), which are used as reference points in the present study. MISP1 and 4 are located near the stagnation point on the windside heatshield, while MISP2, 3, 5, 6 and 7 are located on the leeside of the heatshield. Table 5 provides the coordinates of the different MISP TCs in the MSL computational frame of reference (origin located at the MSL nose).
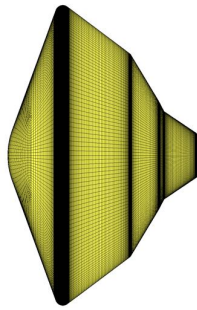
Figure 9: MSL environment mesh.

Figure 11 shows the time evolution of the wall pressure p, heat transfer coefficient C_H, BLE enthalpy h_e, and wall enthalpy h_w at the MISP locations. A linear time interpolation method is used to determine the quantities between discrete trajectory points. The peak of pressure occurs around 84 s (Fig. 11a)
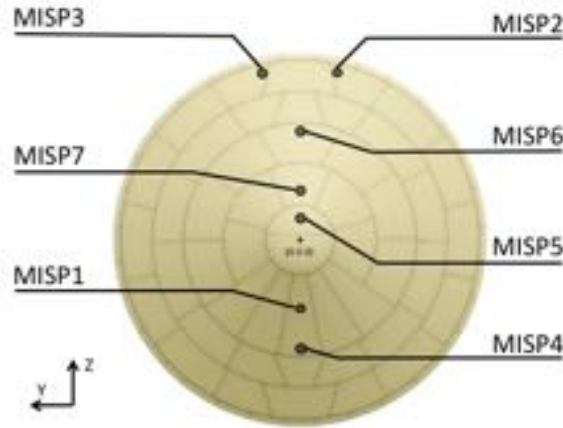
---

[4]https://software.nasa.gov/software/LEW-16851-4

Figure 10: MISP sensor locations.[5]

Table 5: MISP locations.

| MISP	TC	Location [m] (x y z)
MISP1	TC1	(0.22149301 -0.00013062 -0.79915441)
	TC2	(0.22378948 -0.00013044139 -0.7831858)
	TC3	(0.22981382 -0.00012995826 -0.79612625)
	TC4	(0.23573302 -0.00012948343 -0.7939716)
MISP2	TC1	(0.63698311 -0.39981331 1.8991256)
	TC2	(0.63931252 -0.39963837 1.8982953)
	TC3	(0.64525818 -0.39919186 1.8961761)
	TC4	(0.65115686 -0.39874887 1.8940737)
MISP3	TC1	(0.63691597 0.399815228 1.899147)
	TC2	(0.63907595 0.39965305 1.8983771)
	TC3	(0.64534927 0.39918189 1.896141)
	TC4	(0.65099339 0.39875799 1.8941292)
MISP4	TC1	(0.43970427 -0.0002627826 -1.3992174)
	TC2	(0.44245079 -0.00026224322 -1.3982187)
	TC3	(0.4480285 -0.00026217208 -1.3961905)
	TC4	(0.4542552 -0.00026209266 -1.3939263)
MISP5	TC1	(0.020429635 -7e-7 0.19957281)
	TC2	(0.022732818 -1.0621e-6 0.19915667)
MISP6	TC1	(0.38536773 -1.03e-5 1.2491638)
	TC2	(0.38764399 -1.03e-5 1.2483345)
	TC3	(0.39377674 -1.02611e-5 1.246102)
	TC4	(0.39941096 -1.021e-5 1.2440476)
MISP7	TC1	(0.11203581 -4.26e-6 0.4991888)
	TC2	(0.11438964 -4.42e-6 0.49833204)

and is the highest at plugs 1 and 4, close to the stagnation point. Two peaks

appear for the heat transfer coefficient at about 75 s and 85 s. As expected

in laminar flow regime, C_H has the largest value at MISP5 location where the

maximum heating occurs. There are no MISP sensors to record the high heating

expected at the outer flank regions. Figure 11c compares the BLE enthalpy to

the wall enthalpy over time. The two enthalpy profiles approach one another at

about 90 s. At this point in time, the convective heating tends to zero.

(a) Pressure p

(b) Heat transfer coefficient C_H

(c) BLE enthalpy h_e and wall enthalpy h_w
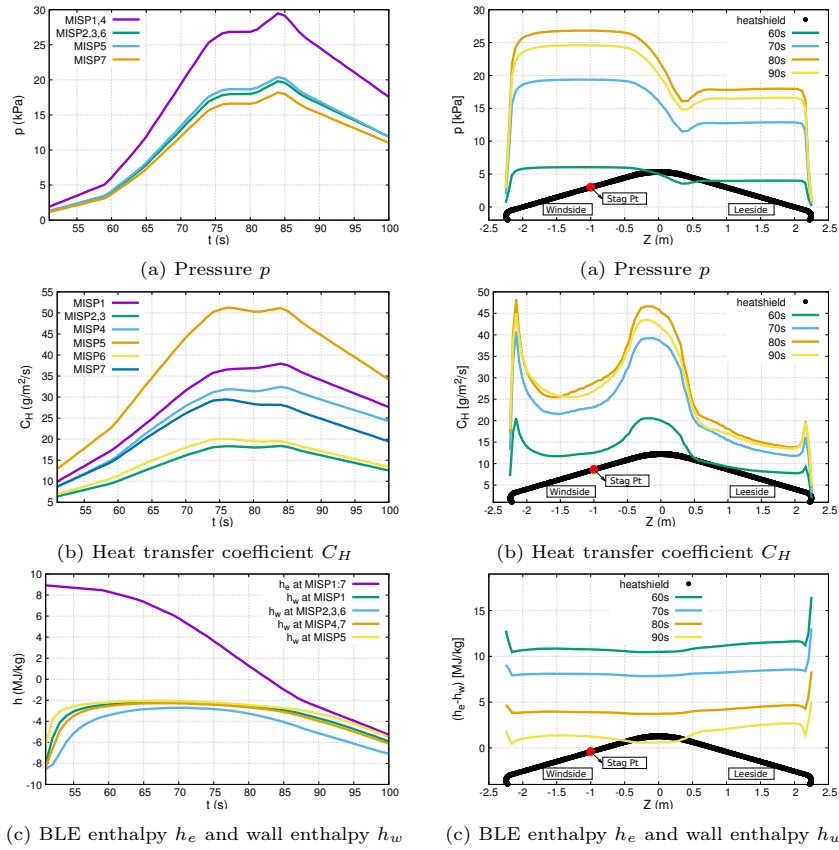
Figure 11: Evolution in time of PATO inputs (p_w, C_H and h_e) at the heatshield front surface (50 to 100 s of MSL entry).

(a) Pressure p

(b) Heat transfer coefficient C_H

(c) BLE enthalpy h_e and wall enthalpy h_w

Figure 12: Cutting plane in Y direction of PATO inputs (p_w, C_H and h_e) at the heatshield front surface (60, 70, 80 and 90 s of MSL entry).

Figure 12 shows quantities along the heatshield surface, on the X-Z symmetry plane. Values of pressure p, heat transfer coefficient C_H, BLE enthalpy

20

h_e and wall enthalpy h_w are shown as a function of entry time. Figure 12a highlights the higher pressure at the windside region and the pressure dip at the nose region. Figure 12b shows two peaks for C_H at the windside outer flank and nose regions. Figure 12c plots the quantity $(h_e - h_w)$ which is directly proportional to the corrected convective heat flux q_{flux}, detailed in Appendix A. This difference approaches zero at 90 s and has the highest value at the outer flank regions. Away from the outer flank regions, the values along the front surface are relatively constant at discrete times. A 3D-view of the heatshield front surface for the quantities of interest is presented in Fig. 13 at 70 s after Entry Interface. Figure 13a shows the pressure distribution on the heatshield, and the location of the stagnation point at the windside forebody. As observed in the 2D profile of Fig. 12b, Figure 13b shows that the heat transfer coefficient peaks at the nose and at the windside outer flank, which are determined by the capsule geometry and entry angle of attack.


(a) Pressure p

(b) Heat transfer coefficient C_H

(c) BLE enthalpy h_e and wall enthalpy h_w
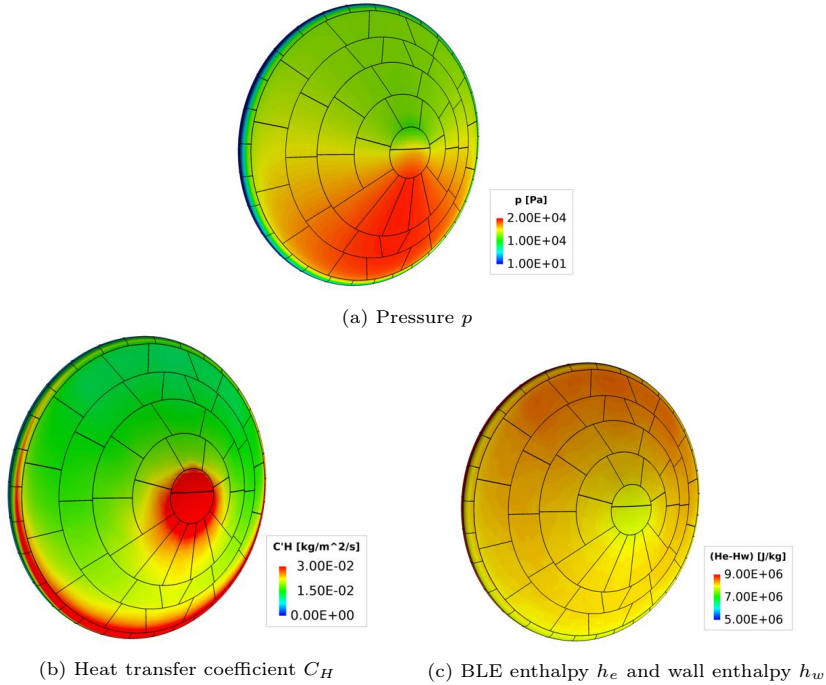
Figure 13: 3D-view of PATO inputs at the heatshield front surface (70 s of MSL entry).

21

4.1. Spatial interpolation

A spatial interpolation procedure was developed to interface the PATO and DPLR grids. While DPLR uses a structured mesh for the computation of the aerothermal environment, PATO adopts an unstructured moving mesh technique for the material response. PATO's moving grid system allows for shape changes due to surface recession. A spatial interpolation between the DPLR and PATO grids is performed at discrete time steps for the different meshes. The Arbitrary Mesh Interface (AMI) of OpenFOAM was used for such purpose. AMI enables interfacing adjacent, disconnected mesh domains using Galerkin projection.[22] Figure 14 shows an illustration of the spatial interpolation for two different regions of the heatshield forebody surface at 90 s of the MSL trajectory. The thick black lines represent the gap filler between two adjacent PICA tiles. The environment grid is presented in pink color, while the material grid is shown in black. It is noticed that, at the outer flank region (Fig. 14a), the cell size of the two grids is similar. In contrast, Figure 14b shows large differences between mesh resolutions at the nose region. This difference causes small numerical fluctuations at the nose region, which are deemed negligible for the present study. Future improvement shall include the capability to adapt the hypersonic CFD grid to better match the porous material response mesh. Figure 14 also shows the surface shape change due to material ablation. The differential recession between the non-receding gap filler and the ablative porous material promotes the formation of a fence. This result closely resembles the fencing phenomenon observed experimentally when testing PICA samples with RTV-bonding interfaces.[5] The fencing phenomenon poses design challenges as it is a potential promoter of transition to turbulence.[23] If a detailed material model for the gap filler were added to the CFD simulation, the current technology would improve prediction models of the fencing phenomenon along a varying heat flux trajectory. However, this is out of the scope of the present article where we focus on modeling the material response with and without tiling the heatshield.

22
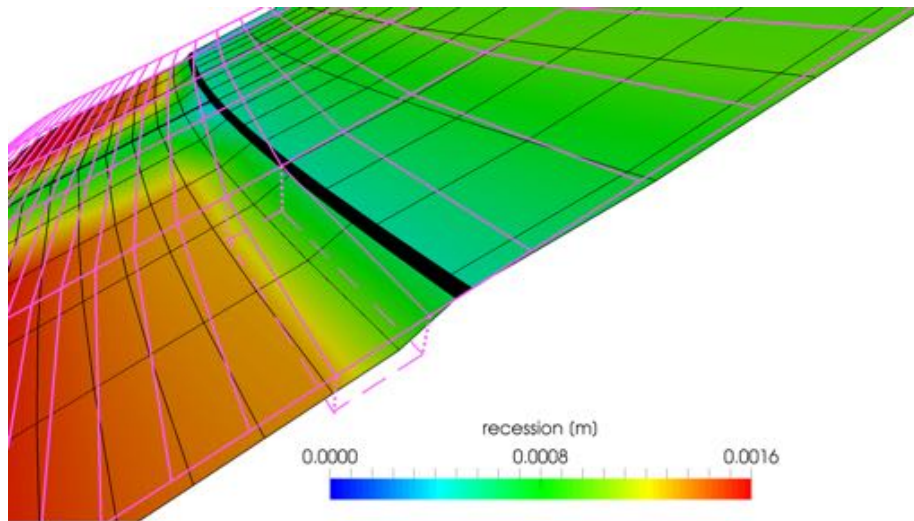
(a) Outer flank region.
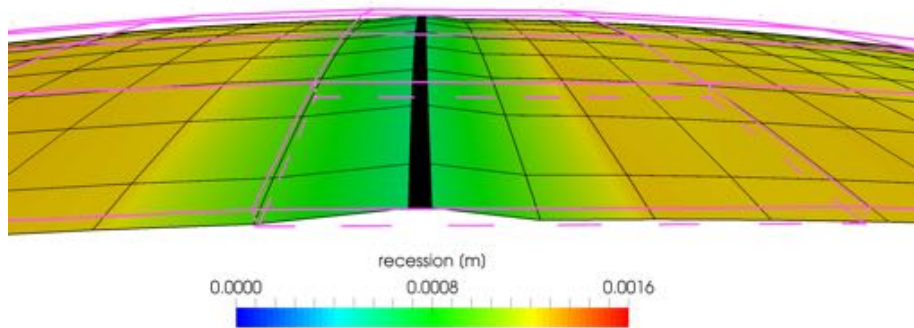
(b) Nose region.

Figure 14: Spatial interpolation between the environment grid (pink) and the material grid (black) at 90 s of MSL entry.
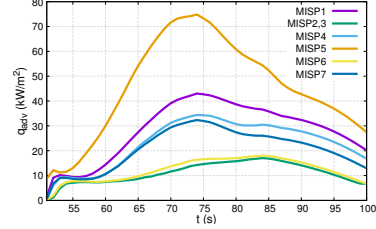
5. Results

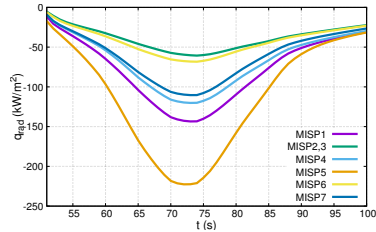### 5.1. Energy fluxes at the heatshield front surface

Figure 15 shows the time evolution of the net corrected convective flux q_{flux},
the net advective flux q_{adv} and the net radiative flux q_{rad} at the MISP locations.
Those quantities are calculated from the inwards and outward contributions
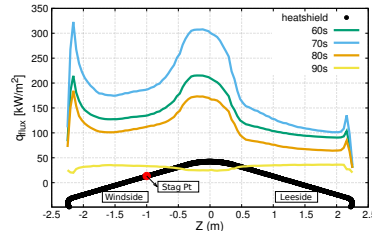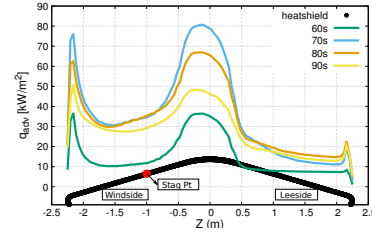formulated in Appendix A.2.
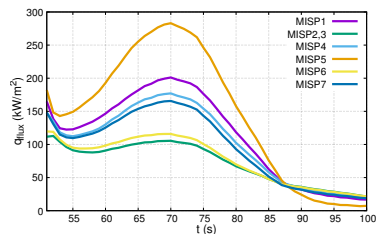
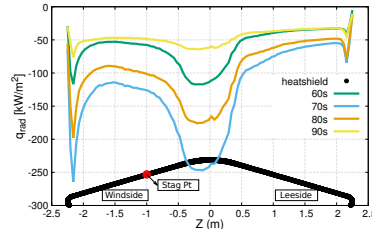(a) Corrected convective flux q_{flux}.

(b) Advective flux q_{adv}.

(c) Radiative flux q_{rad}.

Figure 15: Evolution in time of the energy fluxes at the heatshield front surface (50 to 100 s).

(a) Corrected convective flux q_{flux}.

(b) Advective flux q_{adv}

(c) Radiative flux q_{rad}

Figure 16: Cutting plane in Y direction of the energy fluxes at the heatshield front surface (60, 70, 80 and 90 s of MSL entry).

For the net radiative flux, the contribution q_{pla} from the plasma radiation is
assumed to be small and can be neglected in this simulation. Figure 15a shows
the peak of q_{flux} occurring at about 70 s of MSL entry. The highest value

24

for the MISP5 is a direct consequence of C'_H being the highest at the MISP5 location. The advective flux is less than 40% of the corrected convective flux all along the MSL entry and has a peak about 75 s. Contrary to q_{flux} and q_{adv}, the radiative flux cools down the heatshield front surface under the assumption of no shock radiation.

(a) Corrected convective flux q_{flux}.

(b) Advective flux q_{adv}.

(c) Radiative flux q_{rad}.
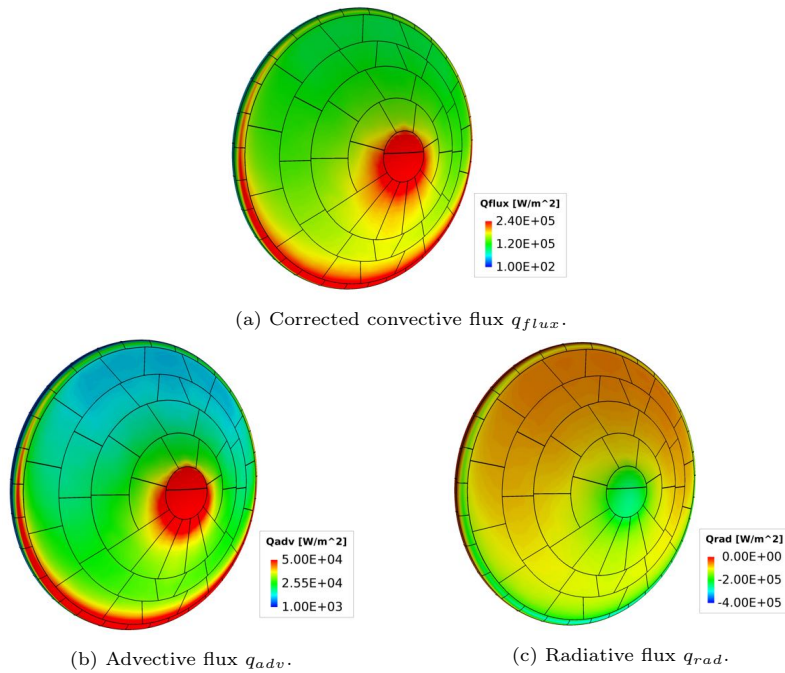
Figure 17: 3D-view of the energy fluxes at the heatshield front surface (70 s of MSL entry).

Figure 16 shows the distribution of the fluxes along the heatshield surface at the X-Z median plane of the body, for different trajectory times. The three fluxes q_{flux}, q_{adv} and q_{rad} have two major peaks at the windside outer flank and nose regions. The highest value of these fluxes occurs at around 70 s. Figure 16a shows that the q_{flux} is nearly constant at 90 s and approaches zero due to the small difference between h_e and h_w (cf. Fig. 11c), as previously explained in section 4. Figure 16b shows q_{adv} has a lower value than q_{flux} most of the time. Figure 16c shows that the radiative cooling peak at the nose is practically null at 90 s. The distribution of the fluxes over the entire surface is shown in

25

Fig. 17 for completeness. The contours are at 70 s entry time.

5.2. Estimated temperature and recession at the heatshield front surface

Similar to the fluxes, computed surface temperature and recession are first shown as a function of time for the 5 MISP locations (Fig. 18), then along the X-Z median plane (Fig. 19) and finally in a 3D-view (Fig. 20).

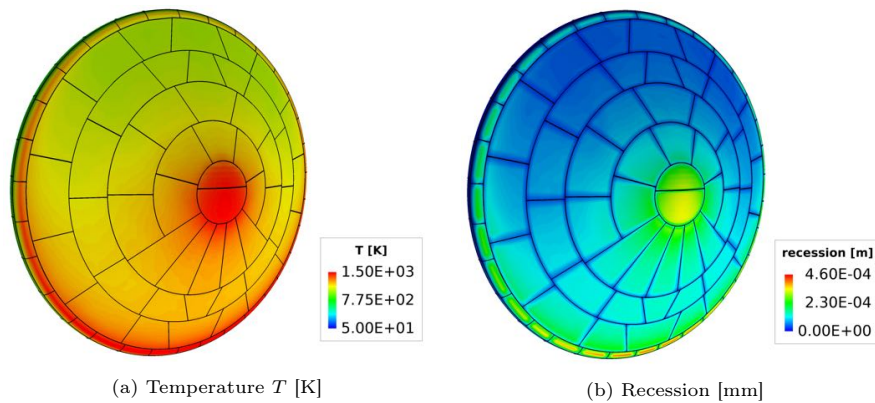(a) Temperature T [K]   (b) Recession [mm]
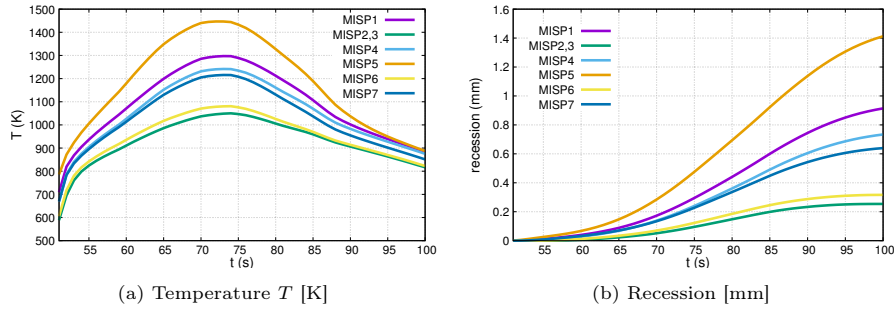
Figure 18: Evolution in time of the temperature and recession at the heatshield front surface (50 to 100 s).

270   The time evolution of the temperature T shows a peak temperature at 70 s which is consistent with the computed fluxes shown in Fig. 15. The temperature is the highest at MISP5, as expected in laminar regime. The predicted recession, shown in Fig. 18b, is in accordance with the computed temperature. The highest recession is 1.4 mm from 50 to 100 s of MSL entry at MISP5. Predicted

275   values are likely different than the actual ones, largely due to a theoretical material model used in the present work and modeling assumptions in the CFD.

(a) Temperature T [K]   (b) Recession [mm]
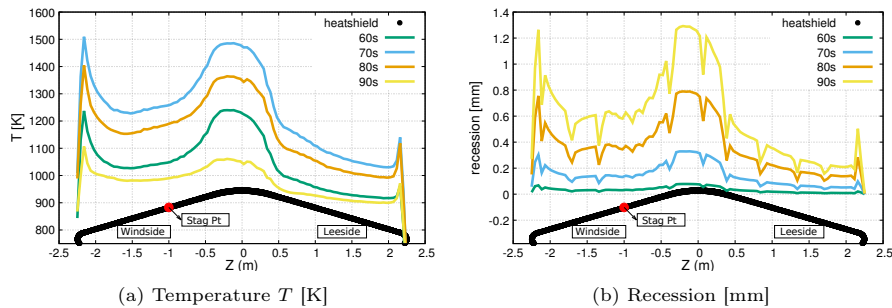
Figure 19: Cutting plane in Y direction of the temperature and recession at the heatshield front surface (60, 70, 80 and 90 s of MSL entry).

26

Nonetheless, values are in line with MSL observations. During the MSL mission, all MISP thermocouples survived the Mars entry. The thermocouple closest to the heatshield surface at the MISP5 location was measured by X-Ray at 2.53mm, which indicates that the maximum recession at that location was less than 2.53mm. Figure 19 shows temperature and recession along the surface on the X-Z median plane at different times. Interestingly, Figure 19b shows an increasing differential recession between the porous material and the tile interface. This is further highlighted in the 3D surface contour in Fig. 20b, for 70 s entry time. Higher temperature regions are observed at the windside outer flank and nose (Fig. 20a) and where a higher recession is predicted as well.

(a) Temperature T [K]   (b) Recession [mm]

Figure 20: 3D-view of the estimated temperature and recession at the heatshield front surface (70 s of MSL entry).

5.3. Tiled configuration analysis

In this section we analyze the effect of tiled configuration on the in-depth 3D velocity and temperature fields. The analysis is based on the assumption that the gap filler within the tiles is impermeable. Results are compared to those obtained using a monolithic material model. The 3D predictions are compared with corresponding 1D solutions, using the same assumptions and models.

5.3.1. Velocity inside the material

²⁹⁵   Figure 21 shows the velocity field inside the heatshield at the leeside, nose and windside regions at 85 s of MSL entry when the maximum stagnation pressure occurs. The in-depth velocity within the porous tiles is chiefly driven by the pressure differences within the tiles, as postulated by Darcy's formulation of the momentum equation (see section 3.2). For the three locations, shown ³⁰⁰ in Fig. 21, we observe an outward velocity normal to the surface, due to the outflow of pyrolysis gases. The transverse velocity is less than 1 mm/s at the leeside flank, at the nose and at the windside flank regions, across the entire heatshield thickness. Such a low transverse velocity suggests that the use of a 1D model is an accurate approximation of the 3D isotropic material behaviour ³⁰⁵ in these regions. Conversely, the velocity at the leeside and windside outer flank regions, where the geometry presents strong curvatures, reaches 0.2 m/s in the transverse direction. In these regions, a 1D model would be unsuitable to correctly predict the flow transport.
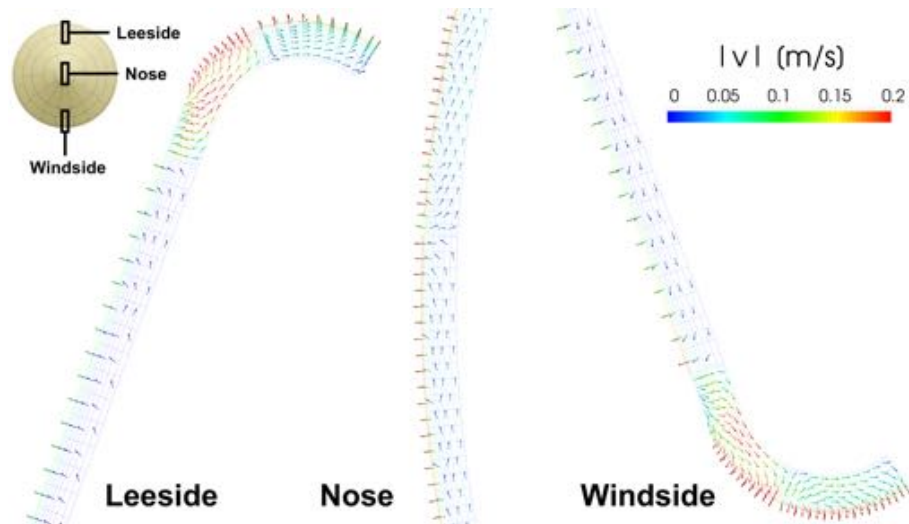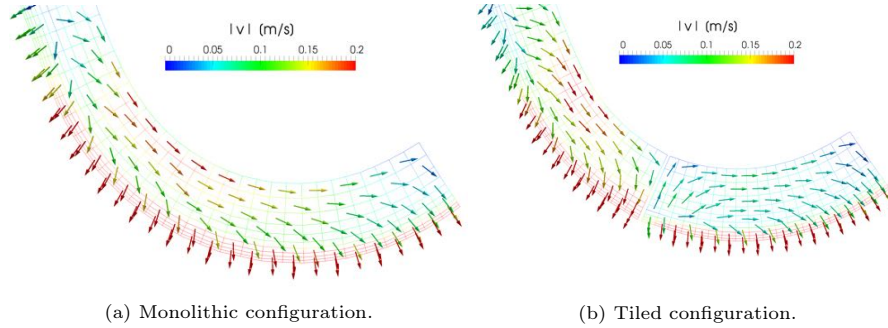

Figure 21: Velocity field at cross-sections of different heatshield regions (85 s of MSL entry).

In Fig. 22, we compare the velocity fields for tiled and monolithic configura- ³¹⁰ tions, at the windside outer flank region. Velocity magnitudes are similar for the
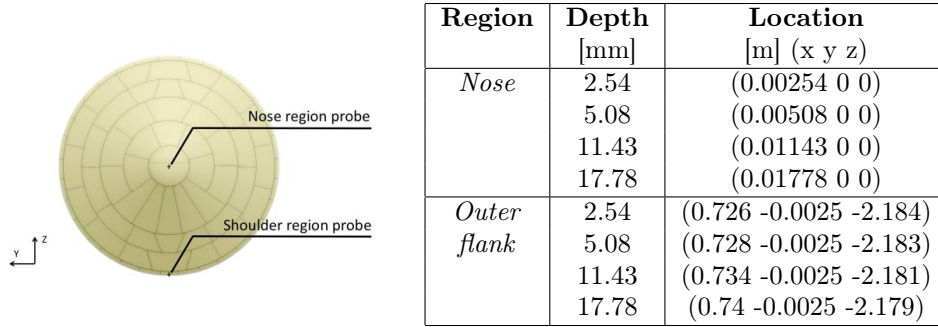
28

two cases, however, one clearly notices that the presence of an impermeable tile causes a strong in-depth velocity swirling, as opposed to the monolithic case, where flow streamlines follow the curvature of the geometry. As a result, we observe regions of gas outflow, as shown in the right tile of Fig. 22b, close to the interface.

(a) Monolithic configuration.   (b) Tiled configuration.

Figure 22: Comparison of the velocity field in different heatshield configurations at a cross-section of the windside region (85 s of MSL entry).

5.3.2. Temperature inside the material

Figure 23 shows the temperature probes locations inside the material.

Region	Depth	Location
	[mm]	[m] (x y z)
Nose	2.54	(0.00254 0 0)
	5.08	(0.00508 0 0)
	11.43	(0.01143 0 0)
	17.78	(0.01778 0 0)
Outer	2.54	(0.726 -0.0025 -2.184)
flank	5.08	(0.728 -0.0025 -2.183)
	11.43	(0.734 -0.0025 -2.181)
	17.78	(0.74 -0.0025 -2.179)

Figure 23: Probes locations.

Figures 24 and 25 show in-depth temperature histories at the nose and at the windside outer flank, respectively. The temperature is plotted at four in-depth positions, for three cases with isotropic material properties: 1D material response, 3D material response with tiles and 3D monolithic material response.

29

The same through-thickness grid resolution is used in the 1D and 3D simulations. A grid convergence study, performed at the probes locations (Fig. 23), showed that the relative difference between the in-depth resolution of 10 and 100 cells is less than 3%. In the nose region (Fig. 24), the three configurations yield very close results. The most pronounced differences are observed at the two most in-depth locations, where the heat transfer is mainly due to conduction in the nose region.
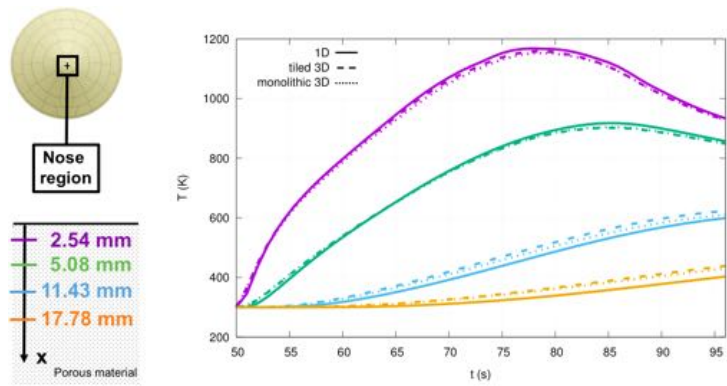

Figure 24: Comparison of the temperature field inside the material for different heatshield configurations at the nose region.
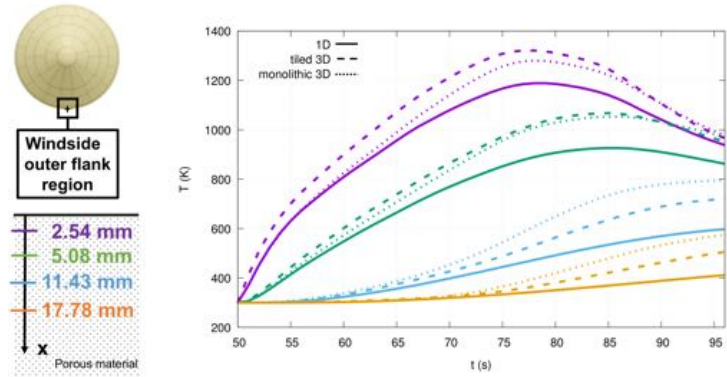

Figure 25: Comparison of the temperature field inside the material for different heatshield configurations at the windside outer flank region.

30

For the windside outer flank (Fig. 25), where 3D flow effects are pronounced, the 1D case underpredicts the temperature beneath the surface by a maximum of 18% compared to the tiled configuration and a maximum of 28% compared to the monolithic configuration. It is expected that, using a transverse anisotropic material properties instead of the isotropic material assumption adopted in the present case, the observed differences would be amplified.

6. Conclusion

In this work we have presented a first three-dimensional material response simulation of the full-scale MSL heatshield, including the tiles architecture. The simulations demonstrated the ability of the modern material response code, PATO, to handle the material response of geometrically complex and large domains, through the use of massively parallel computations. The selected problem served as a test case to optimize the performance of PATO on the NASA Pleiades supercomputer infrastructure.

The DPLR software program was used to compute the hypersonic environment along the MSL entry trajectory for a laminar boundary layer assuming a super-catalytic and non-blowing wall boundary condition. Surface pressure, heat transfer coefficient and enthalpy at the boundary layer edge were extracted from DPLR solutions and used as inputs to PATO. As part of this technology demonstration, we have refined a procedure to project the environmental conditions computed in the hypersonic CFD grid onto a 2 million cells material grid. A linear interpolation scheme in time, and a Galerkin projection in space were proposed to accomplish the projection.

The surface shape change due to the differential recession between the non-receding gap filler and the receding porous material promoted the formation of fences at the tile interface, analogous to the fencing phenomenon observed experimentally in arc-jet tests of PICA samples with RTV-bonding interfaces. The present simulation technology constitutes a first step towards the prediction of the tile interface fencing phenomenon, which is a potential promoter of

transition to turbulence at hypersonic conditions. Realistic finite-rate chemistry models for both PICA and RTV will be fundamental for such predictive effort. Fences can also enhance surface heating for laminar and turbulent flows.

We compared difference between computations for a 3D monolithic heatshield model, a 3D tiled model and a 1D model. Our simulations showed that for the MSL aeroshell geometry, 3D in-depth flow velocity effects are more pronounced at the outer flank region. At the nose and flank regions, where the MISPs sensors are located, the in-depth flow transport is basically one-dimensional since 1D and 3D material response simulations yielded very close results for the in-depth material temperature. This result confirmed the suitability of a 1D model for heatshield sizing purposes and for MISP analysis in those regions. At the outer flank region, where the maximum heating occurs in the laminar regime, the 3D tiled configuration and the 3D monolithic configuration predicted relative differences for in-depth material temperature up to 18% and 28% respectively, when compared to a 1D model. The 1D model underpredicted the temperature at the outer flank when compared to the 3D tiled configuration, and the 3D monolithic model predicted a higher temperature than the 3D tiled model. This prediction can be further refined by adopting a transverse anisotropic material model (e.g. anisotropic effective thermal conductivity and permeability) in future investigations.

Future work will include a strong coupling with the aerothermal environment code, including blowing gases and moving mesh to account for shape changes due to ablation.

Acknowledgements

References

[1] M. J. Wright, R. Beck, K. Edquist, D. Driver, S. Sepka, E. Slimko, W. Will-cockson, T. DeCaro, H. Hwang, Sizing and margins assessment of the Mars Science Laboratory aeroshell thermal protection system, AIAA paper 2009-4231, 2009.

[2] H. K. Tran, C. E. Johnson, D. J. Rasky, F. C. L. Hui, M.-T. Hsu, T. Chen, Y. K. Chen, D. Paragas, L. Kobayashi, Phenolic impregnated carbon ablators (PICA) as thermal protection systems for discovery missions, NASA Technical Memorandum 110440 (1997) 1–70.

[3] M. Stackpoole, S. Sepka, I. Cozmuta, D. Kontinos, Post-flight evaluation of stardust sample return capsule forebody heatshield material, AIAA paper 1202 (2008) 1–7.

[4] M. Mahzari, R. Braun, T. White, D. Bose, Inverse Estimation of the Mars Science Laboratory Entry Aerothermal Environment and Thermal Protection System Response, in: AIAA Thermophysics Conference, 2013.

[5] T. R. White, M. Mahzari, D. Bose, J. A. Santos, Post-flight Analysis of the Mars Science Laboratory Entry Aerothermal Environment and Thermal Protection System Response, in: 44th AIAA Thermophysics Conference, AIAA Paper 2013-2779, San Diego, CA, 2013.

[6] A. D. Omidy, F. Panerai, A. Martin, J. R. Lachaud, I. Cozmuta, N. N. Mansour, Code-to-Code Comparison, and Material Response Modeling of Stardust and MSL using PATO and FIAT, 2015.

[7] Anonymous, Aerotherm charring material thermal response and ablation program - version 3, Tech. rep., Aerotherm report UM-70-14 (1970).

[8] Y. Chen, R. Milos, Ablation and thermal response program for spacecraft heatshield analysis, Vol. 36 of Journal of Spacecraft and Rockets, American Inst. of Aeronautics and Astronautics, 1999.

[9] Y.-K. Chen, F. S. Milos, Multidimensional Effects on Heatshield Thermal Response for the Orion Crew Module, in: 39th AIAA Thermophysics Conference, AIAA Paper 2007-4397, Miami, FL, 2007.

[10] Y.-K. Chen, F. S. Milos, Three-dimensional ablation and thermal response simulation system, Vol. 5064 of AIAA paper, 2005.

[11] D. J. Kinney, Aero-thermodynamics for conceptual design, AIAA Paper 13382, 2004.

[12] J. Lachaud, N. N. Mansour, Porous material analysis toolbox based on OpenFoam and applications, Journal of Thermophysics and Heat Transfer 28 (2) (2014) 191–202.

[13] M. J. Wright, T. White, N. Mangini, Data Parallel Line Relaxation (DPLR) Code User Manual: Acadia-Version 4.01.1, 2009.

[14] K. T. Edquist, A. A. Dyakonov, M. J. Wright, C. Y. Tang, Aerothermodynamic Design of the Mars Science Laboratory Heatshield, in: 41st AIAA Thermophysics Conference, AIAA Paper 2009-4075, San Antonio, Texas, 2009.

[15] J. Lachaud, J. B. Scoggins, T. E. Magin, M. G. Meyer, N. N. Mansour., A generic local thermal equilibrium model for porous reactive materials submitted to high temperatures, Vol. 108 of International Journal of Heat and Mass Transfer, 2017, pp. 1406–1417.

[16] J. B. Scoggins, T. E. Magin, Development of Mutation++: Multicomponent Thermodynamic and Transport Properties for Ionized Plasmas written in C++, in: 11th AIAA/ASME Joint Thermophysics and Heat Transfer Conference, AIAA Paper 2014-2966, Atlanta, GA, 2014.

[17] J. Lachaud, T. van Eekelen, J. B. Scoggins, T. E. Magin, N. N. Mansour, Detailed chemical equilibrium model for porous ablative materials, International Journal of Heat and Mass Transfer 90 (2015) 1034–1045.

34

[18] F. Panerai, J. D. White, T. J. Cochell, O. M. Schroeder, N. N. Mansour, M. J. Wright, A. Martin, Experimental measurements of the permeability of fibrous carbon at high-temperature, International Journal of Heat and Mass Transfer 101 (2016) 267 – 273.

[19] A. Borner, F. Panerai, N. N. Mansour, High temperature permeability of fibrous materials using direct simulation Monte Carlo, International Journal of Heat and Mass Transfer 106 (2017) 1318 – 1326.

[20] K. T. Edquist, A. A. Dyakonov, M. J. Wright, C. Y. Tang, Aerothermodynamic environments definition for the Mars Science Laboratory entry capsule, Vol. 1206 of AIAA paper, 2007, pp. 8–11.

[21] R. A. Mitcheltree, P. A. Gnoffo, Wake flow about a MESUR Mars entry vehicle, Vol. 1958 of AIAA paper, 1994.

[22] P. Farrell, J. Maddison, Conservative interpolation between volume meshes by local Galerkin projection, Vol. 200 of Computer Methods in Applied Mechanics and Engineering, Elsevier, 2011, pp. 89–100.

[23] K. T. Edquist, B. R. Hollis, C. O. Johnston, D. Bose, T. R. White, M. Mahzari, Mars Science Laboratory Heatshield Aerothermodynamics: Design and Reconstruction, Journal of Spacecraft and Rockets, American Institute of Aeronautics and Astronautics, 2014.

[24] M. R. Wool, Aerotherm Equilibrium Surface Thermochemistry Computer Program, Version 3, Volume 1, Program Description and Sample Problems, 1970.

[25] A. Martin, S. C. C. Bailey, F. Panerai, R. S. C. Davuluri, H. Zhang, A. R. Vazsonyi, Z. S. Lippay, N. N. Mansour, J. A. Inman, B. F. Bathel, S. C. Splinter, P. M. Danehy, Numerical and experimental analysis of spallation phenomena, CEAS Space Journal 8 (4) (2016) 229–236.

35

[26] C. B. Moyer, M. R. Wool, Aerotherm Charring Material Thermal Response and Ablation Program, Version 3, Volume 1, Program Description and Sample Problems, Tech. rep., Aertoherm Corp Mountain View CA (1970).

Appendix A. Surface boundary conditions

This appendix summarizes the state-of-the art ablative material boundary conditions [24] implemented in PATO [17] and details the input dataset used for the simulation presented in this document.

Adiabatic and impermeable boundary conditions are used at the material bondline. At the material front surface, a one-dimensional convective boundary condition is used on each mesh face to model heat and mass transfer phenomena from the boundary layer edge to the material surface. The heat and mass transfer coefficients are interpolated from the three-dimensional hypersonics CFD simulations for each external face of the material mesh. On each face, reactive surface mass balance and surface energy balance are resolved to compute the material ablation rate and wall temperature. Surface pressure is directly obtained from the CFD simulations.

Appendix A.1. Surface mass balance

The char ablation rate $\dot{m}_{ca}$ and the wall enthaply h_w are computed with a thermochemical model in equilibrium at the wall.[24] Figure A.26 provides a schematic for the surface mass balance model based on the steady state element conservation in a control volume close to the wall. The equilibrium chemistry in the control volume is assumed to be quasi-steady in order to decouple the material response and the boundary layer. The time variation of p_w, T_w, $\dot{m}_{pg}$ and $\dot{m}_{ca}$ is neglected. Mechanical erosion, which is a phenomenon under investigation [25], is not considered here.

Under the assumption that Prandtl and Lewis numbers are equal to unity and the diffusion coefficients are identical between elements, the conservation of mass fraction of element k in the control volume may be written as

$$C'_H \left(z_{k,w} - z_{k,e}\right) + \left(\dot{m}_{pg} + \dot{m}_{ca}\right) z_{k,w} = \dot{m}_{pg}\ z_{k,pg} + \dot{m}_{ca}\ z_{k,ca} \qquad \text{(A.1)}$$
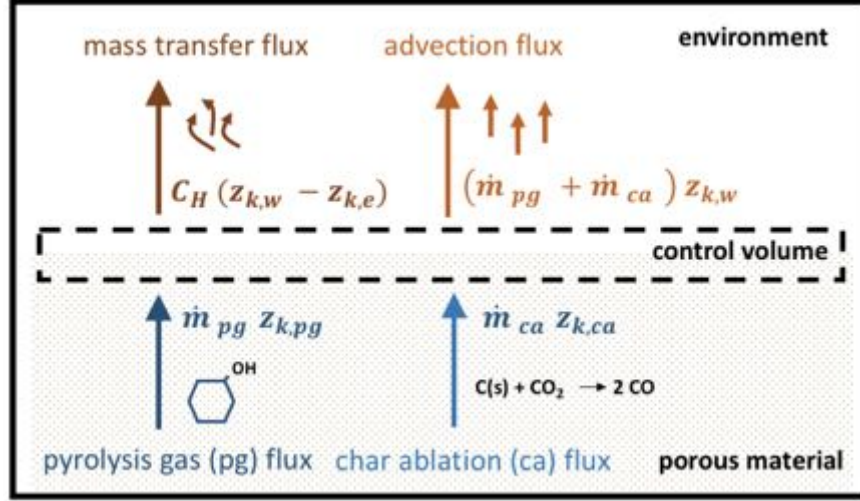
37

Figure A.26: Surface mass balance at the heatshield front surface.

The formation of the species S_i from the elements A_k is formulated as follows

$$S_i \rightleftharpoons \sum_{k \in [1, N_e]} \nu_{i,k} A_k \tag{A.2}$$

Table A.6 shows an example of the formation of the CO_2 specie from the C and O elements.

Table A.6: Example of CO_2 formation in Eq. A.2.

S_1	$\nu_{1,1}$	$\nu_{1,2}$	E_1	E_2
CO_2	1	2	C	O

If the species are assumed perfect gas then the chemical equilibrium is given by

$$\frac{x_i}{\prod_{k \in [1, N_e]} (x_k)^{\nu_{i,k}}} = K_i(T) \Leftrightarrow ln(x_i) - \sum_{k \in [1, N_e]} \nu_{i,k} ln(x_k) - ln[K_i(T)] = 0 \tag{A.3}$$

$$\sum_{i \in [1, N_s]} x_i = 1 \qquad \sum_{k \in [1, N_e]} x_k = 1 \tag{A.4}$$

38

The surface mass balance model computes $\dot{m}_{ca}$ and h_w from Eq. A.1, A.3 and A.4 using the following inputs: C'_H, $\dot{m}_{pg}$, p_w, T_w, $z_{k,e}$, $z_{k,pg}$ and $z_{k,ca}$. The pyrolysis gas production rate at the heatshield front surface $\dot{m}_{pg}$ is computed from Eq. 2 by integrating the pyrolysis, mass and transport equations as explained in section 3. p_w and C_H are given by the aerothermal environment presented in section 4. T_w and C'_H are computed in the surface energy balance described in Appendix A.2. Table A.7 gives the elemental mass fractions $z_{k,e}$, $z_{k,pg}$ and $z_{k,ca}$ used in this work.

Table A.7: Elemental mass fraction inputs of the surface mass balance model.

Elements	$z_{k,e}[-]$	$z_{k,pg}[-]$	$z_{k,ca}[-]$
C	0.3276	0.206	1
H	0	0.6790	0
O	0.6556	0.115	0
N	0.0118	0	0
AR	0.0005	0	0

The material mass loss rate leads to a surface ablation velocity given by

$$\mathbf{v}_{ca} = \frac{\dot{m}_{ca}}{\rho_{sw}}\ \mathbf{n} \tag{A.5}$$

and applied as a mesh motion in PATO.

Appendix A.2. Surface energy balance

The wall temperature T_w is computed with a surface energy balance model [26], as illustrated in Fig. A.27. Heating and cooling energy fluxes from the environment and the porous material are shown. The state-of-the-art surface energy balance at the wall is given by

$$q_{cond}^{out} = C'_H \left(h_e - h_w \right) + \dot{m}_{pg}h_{pg} + \dot{m}_{ca}h_{ca} - \left(\dot{m}_{pg} + \dot{m}_{ca} \right) h_w + q_{rad}^{in} - \varepsilon_w \sigma T_w^4 \tag{A.6}$$
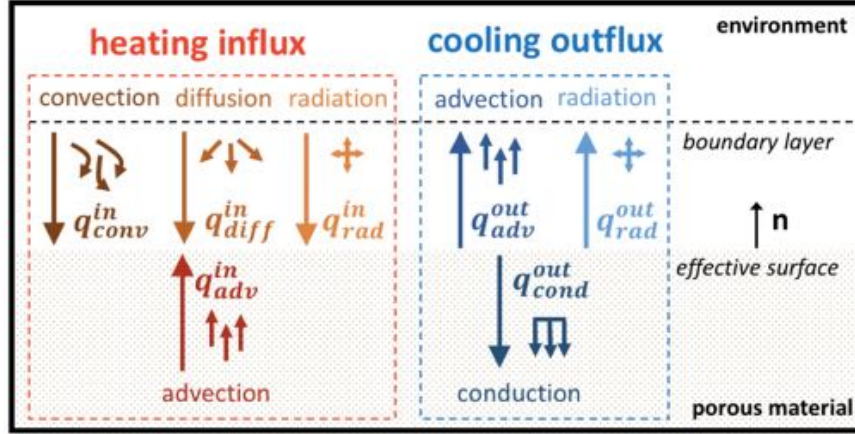
39

Figure A.27: Surface energy balance at the heatshield front surface.

The equality between inward and outward fluxes yields

$$q_{conv}^{in} + q_{diff}^{in} + q_{rad}^{in} + q_{adv}^{in} = q_{cond}^{out} + q_{rad}^{out} + q_{adv}^{out} \tag{A.7}$$

The different terms of Eq. A.7 are formulated here. The convective heat flux, under the assumption of a frozen boundary layer and a non-catalytic wall is

$$q_{conv}^{in} = C_H \left(h_e - h_{ew} \right) \tag{A.8}$$

h_{ew} is the enthalpy computed at the wall temperature, with the *boundary layer edge* gaseous species composition.

$$h_{ew} = \sum_{i \in [1,N_s]} y_{i,e} h_i(T_w) \tag{A.9}$$

The energy carried by diffusion of the gaseous species is given by

$$q_{diff}^{in} = C_M \left(h_{ew} - h_w \right) \tag{A.10}$$

h_w is the enthalpy at the wall temperature, with the *porous material* gaseous

species composition.

$$h_w = \sum_{i \in [1, N_s]} y_{i,w} h_i(T_w) \tag{A.11}$$

The advective energy transport produced by the pyrolysis and the char ablation read respectively

$$q_{adv}^{in} = \dot{m}_{pg} h_{pg} + \dot{m}_{ca} h_{ca} \tag{A.12}$$

$$q_{adv}^{out} = (\dot{m}_{pg} + \dot{m}_{ca}) h_w \tag{A.13}$$

The radiative heating from the plasma is given by

$$q_{rad}^{in} = \alpha_w \, q_{pla} + \varepsilon_\infty \, \sigma \, T_\infty^4 \tag{A.14}$$

while the re-radiative cooling by surface emission reads

$$q_{rad}^{out} = \varepsilon_w \, \sigma \, T_w^4 \tag{A.15}$$

under the assumption that the surface behaves as a gray body.

The effective heat conduction in the porous material is given by

$$q_{cond}^{out} = -\left(\bar{\bar{\mathbf{k}}}_w \cdot \frac{\partial T_w}{\partial \mathbf{n}} \right) \cdot \mathbf{n} \tag{A.16}$$

Eq. A.7, using the different energy contributions explained above, gives

$$-\left(\bar{\bar{\mathbf{k}}}_w \cdot \frac{\partial T_w}{\partial \mathbf{n}} \right) \cdot \mathbf{n} = C_H \left(h_e - h_{ew} \right) + C_M \left(h_{ew} - h_w \right)$$
$$+ \dot{m}_{pg} \left(h_{pg} - h_w \right) + \dot{m}_{ca} \left(h_{ca} - h_w \right) - \varepsilon_w \sigma \left(T_w^4 - T_\infty^4 \right) + \alpha_w q_{pla} \tag{A.17}$$

Assuming equal Prandtl and Lewis number and equal diffusion coefficients for all elements, Eq. A.17 becomes

$$-\left(\bar{\bar{\mathbf{k}}}_w \cdot \frac{\partial T_w}{\partial \mathbf{n}} \right) \cdot \mathbf{n} = C_H' \left(h_e - h_w \right)$$
$$+ \dot{m}_{pg} \left(h_{pg} - h_w \right) + \dot{m}_{ca} \left(h_{ca} - h_w \right) - \varepsilon_w \sigma \left(T_w^4 - T_\infty^4 \right) + \alpha_w q_{pla} \tag{A.18}$$

C_H is corrected to account only for the blockage induced by the pyrolysis and ablation gas blowing. Other film coefficient corrections, such as roughness and hot wall effects, are not considered in this study. The following correction is used with the scaling factor λ equals to 0.5.[8]

$$C'_H = C_H \frac{ln\left[1 + 2\lambda\left(B'_{pg} + B'_{ca}\right)\right]}{2\lambda\left(B'_{pg} + B'_{ca}\right)} \tag{A.19a}$$

$$B'_{pg} = \frac{\dot{m}_{pg}}{C_M} \tag{A.19b}$$

$$B'_{ca} = \frac{\dot{m}_{ca}}{C_M} \tag{A.19c}$$

The surface energy balance computes T_w from Eq. A.18 using the following inputs: C'_H, h_e, h_w, $\dot{m}_{pg}$, h_{pg}, $\dot{m}_{ca}$, h_{ca}, ε_w, T_∞, α_w and q_{pla}. C'_H is computed with Eq. A.19. C_H and h_e are given by the aerothermal environment presented in Section 4. h_w and $\dot{m}_{ca}$ come from the surface mass balance. $\dot{m}_{pg}$ is computed by integrating the pyrolysis, mass and transport equations as explained in section 3. h_{pg} and h_{ca} are computed using the Mutation++ library.[16] Table A.8 shows the other inputs of the surface energy balance.

Table A.8: Inputs of the surface energy balance model.

$\lambda[-]$	$\varepsilon_v[-]$	$\varepsilon_c[-]$	$\alpha_v[-]$	$\alpha_c[-]$	q_{pla} [W/m^2]	T_∞ [K]
0.5	0.8	0.9	0.8	0.9	0	200